Journal of Solid State Chemistry 182 (2009) 1538–1544

Contents lists available at ScienceDirect

Journal of Solid State Chemistry

journal homepage: www.elsevier.com/locate/jssc

Synthesis and characterization of rare-earth doped $SrBi_2Nb_2O_9$ phase in lithium borate based nanocrystallized glasses

B. Harihara Venkataraman [a], Takumi Fujiwara [b], Takayuki Komatsu [a,*]

[a] Department of Materials Science and Technology, Nagaoka University of Technology, 1603-1 Kamitomioka-cho, Nagaoka 940-2188, Japan
[b] Department of Applied Physics, Graduate School of Engineering, Tohoku University, Sendai 980-8579, Japan

ARTICLE INFO

Article history:
Received 11 February 2009
Received in revised form
1 April 2009
Accepted 2 April 2009
Available online 9 April 2009

PACS:
61.46.Hk
78.30.−j
81.05.−t
81.05.Kf

Keywords:
Strontium bismuth samarium niobate
Perovskite like phase
Nanocrystallites
Glass
Micro-Raman spectra
Dielectric constant

ABSTRACT

Glass composites comprising of un-doped and samarium-doped $SrBi_2Nb_2O_9$ nanocrystallites are fabricated in the glass system $16.66SrO–16.66[(1-x)Bi_2O_3–xSm_2O_3]–16.66Nb_2O_5–50Li_2B_4O_7$ ($0 \leqslant x \leqslant 0.5$, in mol%) via the melt quenching technique. The glassy nature of the as-quenched samples is established by differential thermal analyses. Transmission electron microscopic studies reveal the presence of about 15 nm sized spherical crystallites of the fluorite-like $SrBi_{1.9}Sm_{0.1}Nb_2O_9$ phase in the samples heat treated at 530 °C. The formation of layered perovskite-type un-doped and samarium-doped $SrBi_2Nb_2O_9$ nanocrystallites with an orthorhombic structure through the intermediate fluorite phase is confirmed by X-ray powder diffraction and micro-Raman spectroscopic studies. The influence of samarium doping on the lattice parameters, lattice distortions, and the Raman peak positions of $SrBi_2Nb_2O_9$ perovskite phase is clarified. The dielectric constants of the perovskite $SrBi_2Nb_2O_9$ and $SrBi_{1.9}Sm_{0.1}Nb_2O_9$ nanocrystals are relatively larger than those of the corresponding fluorite-like phase and the precursor glass.

1. Introduction

Nanocrystalline materials have immense potential for a variety of applications, by virtue of their electrical, magnetic, and optical properties [1]. They are attractive not only for their potential for technological applications, but also the feasibility which they provide to engineer their structures at atomic levels to generate solids with novel properties [2,3]. Recently, glass nanocomposites comprising nanocrystallites of ferroelectric materials embedded in glass matrices form an important class of polar materials, and also it has been considered as one of the effective methods for fabricating nanomaterials. Ferroelectric crystallites of nano to micrometer sized dispersed in a glassy matrix were known to exhibit electro-optic [4] and non-linear optical properties such as second harmonic generation [5,6]. Various attempts to synthesize glass–ceramic nano/micro composites for a wide range of device applications, which include large area pyroelectric detectors, actuators, frequency doublers, and electro-optic modulators, have been carried out so far. For instance, nanocrystallizations of $Ba_2TiSi_2O_8$, $Ba_2TiGe_2O_8$, $Bi_2VO_{5.5}$, and Bi_2WO_6 in glass matrices have been fabricated [7–10].

In recent years, bismuth-based, layer-structured perovskites such as $SrBi_2Nb_2O_9$ (SBN) and $SrBi_2Ta_2O_9$ (SBT) have been investigated extensively, because of their potential use in ferroelectric random access memories (FeRAMs) [11–13]. $SrBi_2Nb_2O_9$ belongs to the $n = 2$ member of the bismuth layered ferroelectric family of oxides and the crystal structure of SBN comprises of $(Bi_2O_2)^{2+}$ layers interleaved with pseudo-perovskite blocks $(A_{n-1}B_nO_{3n+1})^{2-}$, where *A*-site and *B*-site are occupied by Sr^{2+} and Nb^{5+} ions, respectively, and *n* represents the number of octahedral layers. In comparison with non-layered perovskite ferroelectrics such as $Pb(Zr,Ti)O_3$, these offer several advantages such as fatigue free, lead free, low operating voltages, and most importantly their ferroelectric properties are independent of film thickness in the 90–500 nm range [14,15]. For FeRAM device applications, large remnant polarization (P_r), low coercive field (E_c) accompanied by high Curie temperature (T_c) are required for better performance and reliable operation. Much effort has been made to enhance the ferroelectric properties of SBN ceramics by substitution of the Bi^{3+} ion by alternate cations [16,17]. Srinivas et al. [18] studied the effect of rare-earth ions (Sm^{3+}) on the bismuth site and found that the physical properties of the SBN ceramics have been enhanced.

* Corresponding author. Fax: +81 258 47 9300.
E-mail address: komatsu@mst.nagaokaut.ac.jp (T. Komatsu).

0022-4596/$ - see front matter © 2009 Elsevier Inc. All rights reserved.
doi:10.1016/j.jssc.2009.04.004

Since the preparation and characterization of nanocrystalline materials have nowadays become increasingly important owing to their improved physical properties, an attempt to synthesize nanocrystallites of samarium-doped SBN by glass nanocrystal composite route would be of great interest. Therefore, we studied the glass formation in the system of $16.66SrO–16.66[(1-x)Bi_2O_3 - xSm_2O_3]–16.66Nb_2O_5–50Li_2B_4O_7$ ($0 \leqslant x \leqslant 0.5$, in mol%) and evolutions of the nanocrystalline un-doped and samarium-doped SBN phase along with the structural and dielectric properties in this paper. It is known that lithium borate $Li_2B_4O_7$ (LBO) glass is a suitable host glass matrix for dispersing layer-structured ferroelectric oxides belonging to the Aurivillius family of oxides by virtue of its favorable structural, thermal, and optical properties [9,10].

2. Experimental

Transparent glasses in the composition $16.66SrO–16.66[(1-x)Bi_2O_3–xSm_2O_3]–16.66Nb_2O_5–50Li_2B_4O_7$ ($x = 0–0.5$ mol%) were fabricated by the conventional melt quenching technique. Well mixed powders containing appropriate amounts of reagent grade $SrCO_3$, Bi_2O_3, Sm_2O_3, Nb_2O_5, and $Li_2B_4O_7$ have been taken in molar ratios and were melted in a platinum crucible at 1300 °C for 1 h in an electric furnace. The melts were well shaken intermittently to ensure the homogeneity and to prevent from the formation of air bubbles. A pair of iron blocks, maintained at a temperature of 150 °C, was used to quench the melts into plates with 1.5 mm thickness, and subsequently the as-quenched samples were annealed at 400 °C for 6 h, at a heating rate of 10 K min^{-1} and a cooling rate of 1 K min^{-1} to anneal out any thermal stresses that are likely to exist. Differential thermal analyses (DTA) were employed on these samples in the 30–1000 °C temperature range and with a heating rate of 10 K min^{-1} in order to assess the glass transition (T_g) and crystallization temperatures (T_P). The weight of the sample was the same ($\approx$10 mg) for all the glass compositions under study.

The as-quenched glasses and the samples heat treated at various temperatures were subjected to X-ray powder diffraction (XRD) studies at room temperature using Cu$K\alpha$ radiation to confirm their amorphous and crystalline nature. High resolution transmission electron microscopic (HRTEM) along with the selected area electron diffraction (SAED) studies were carried out to examine the amorphous/crystalline states of the powders of the as-quenched glass (annealed: 400 °C/6 h) and the heat treated (530 °C/3 h) samples. Optical transmission spectra were recorded in the wavelength range of 190–1100 nm by using the Shimazu UV-3150 spectrometer. Micro-Raman scattering spectra at room temperature for the as-quenched glass and crystallized samples were measured by using a laser microscope operated at 488 nm wavelength (Ar^+ laser). In the micro-Raman experimental set up, the Raman scattering intensity could not be measured below the wavenumber of 250 cm^{-1} because of the use of an edge filter. The capacitance measurements were performed by using an HP 4192A impedance analyzer. Polished plates of the heat treated samples were electroded on both the sides by using silver epoxy and dried at room temperature for 1 h to make the capacitance measurements. The dielectric constant at the frequency of 100 kHz at room temperature was calculated based on the capacitance, electrode area and the sample thickness.

3. Results and discussion

3.1. Thermal analyses

The DTA patterns for the as-quenched samples are shown in Fig. 1. The shapes of all the curves are similar and confirm the glassy nature of all the as-quenched samples. The exotherms in the temperature range 500–670 °C correspond to the crystallization, and the peak positions are defined as crystallization peak temperatures of T_P, T_{P1}, and T_{P2}. The magnitude of the first exotherm (T_P) is lower than that of the second exotherm (T_{P1}) in all the range of compositions under study. The endotherms corresponding to the glass transition (T_g) are observed at 460–480 °C, even though some of these DTA patterns indicate endotherms with small magnitudes (which would be perhaps masked by the first exotherm). The endotherms that are encountered around 830 °C are due to the melting of the glass composite. The values of T_g, T_P, and T_{P1} obtained from DTA patterns are shown in Fig. 2. The glass transition temperature increases with increasing Sm_2O_3 content, suggesting that the presence of Sm_2O_3 in the present glass system decreases the contribution from the non-bridging oxygen. It is found that the first crystallization peak temperature T_P increases almost linearly with the increase in Sm_2O_3 content, while the second crystallization peak temperature T_{P1} seems to be almost constant.

The compositional dependence of the thermal stability factor, i.e., $\Delta T = T_x - T_g$, is also included in Fig. 2, where T_x is the crystallization onset temperature. It increases rapidly with increasing Sm_2O_3 content, which proves that the glass system of $16.66SrO–16.66[(1-x)Bi_2O_3–xSm_2O_3]–16.66Nb_2O_5–50Li_2B_4O_7$, i.e., the whole SBN–LBO binary system, is a potential stable glass forming system. The stability of the glasses could also be predicted by the factor T_g/T_m, i.e., the ratio of the glass transition and melting (T_m) temperatures. For very stable glasses the ideal value of T_g/T_m is 0.67 [19]. The T_g/T_m values of all the compositions studied in the present study fall in the range 0.55–0.58, being close to that of the ideal value.

3.2. Structural and microstructural analyses

The XRD studies were carried out on the as-quenched and the heat treated samples to confirm their amorphous and crystalline

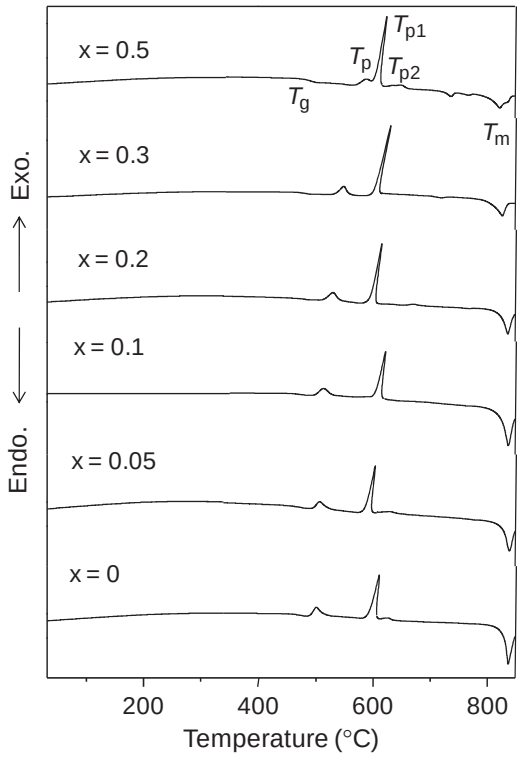

Fig. 1. DTA patterns for the as-quenched glasses of all the compositions.

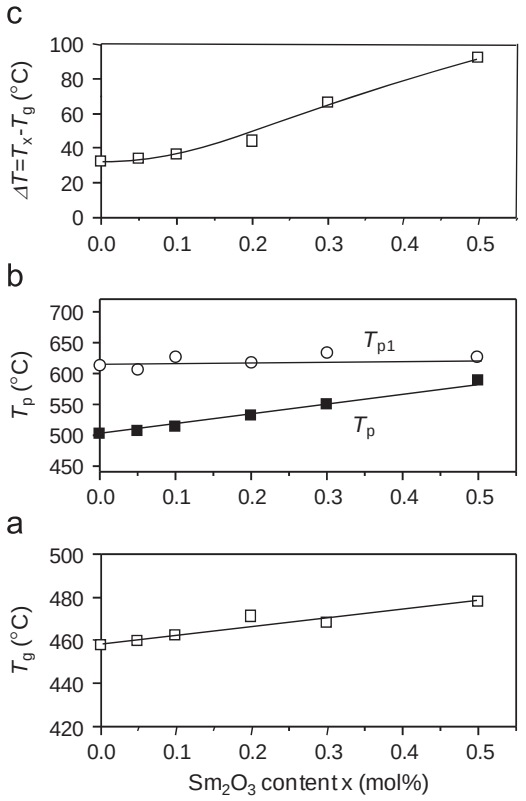

Fig. 2. Compositional dependence of (a) glass transition temperature (T_g), (b) crystallization temperatures (T_p), and (c) thermal stability factor (ΔT).

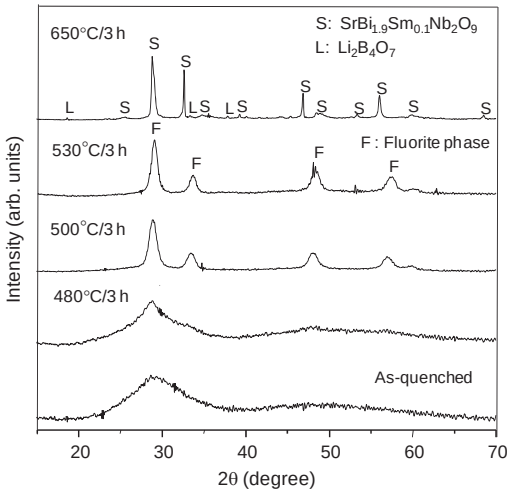

Fig. 3. XRD patterns at room temperature for the as-quenched and the heat treated glass samples of the composition $x = 0.1$.

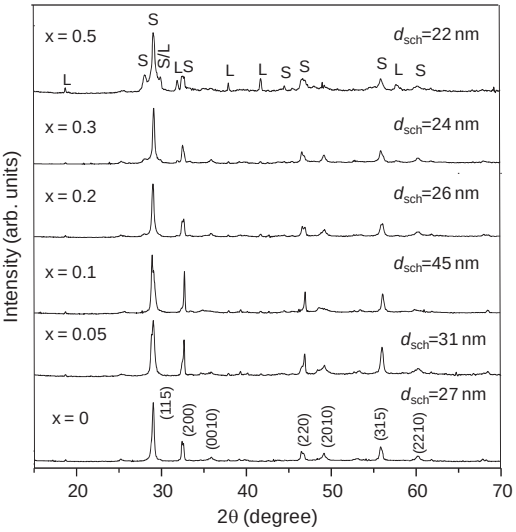

Fig. 4. XRD patterns at room temperature for the samples heat treated at 650 °C for 3 h of various compositions. $S = SrBi_{2-x}Sm_xNb_2O_9$ and $L = Li_2B_4O_7$.

nature, respectively. As an example, the XRD patterns obtained for the sample with $x = 0.1$ are shown in Fig. 3. A broad hump is noticed for the as-quenched and heat treated (480 °C) samples and no distinct peaks are observed, suggesting the amorphous nature of the samples. The XRD patterns for the samples heat treated at 500 and 530 °C (i.e., the vicinity of T_p) show the clear Bragg peaks, indicating the formation of crystals. The *d*-spacings (0.3084, 0.2671, 0.1887, and 0.1609 nm) that are associated with these crystalline peaks are in agreement with those reported in the literature for the fluorite phase of SBN [20]. The monophasic formation of the $SrBi_{1.9}Sm_{0.1}Nb_2O_9$ (SBSmN) fluorite-like phase clearly demonstrates the successful substitution of samarium in SBN lattice. It is interesting to note in these patterns that the diffraction peaks are fairly broad, which are attributed to the presence of very fine crystallites of the fluorite-like SBSmN phase. Indeed, these samples are transparent in the visible wavelength region showing an absorption edge at a wavelength of $\lambda = 408$ nm and thus confirming the fine size of the embedded crystallites. Furthermore, the transmission electron micrographs recorded on the sample heat treated at 530 °C clearly reveal the formation of the nanocrystallites consisting of fluorite-like SBSmN phase with a diameter of about 15 nm (which is in the same range as that obtained by XRD analyses). The details of transmission electron microscope (TEM) observations will be elucidated later in this paper.

The Bragg peaks appeared for the sample heat treated at 650 °C (i.e., the vicinity of T_{P1}) are assigned to the perovskite SBSmN [21] and LBO crystalline phases. These results imply that the second exotherm in Fig. 1 is associated with both the crystallization of perovskite un-doped and samarium-doped SBN phase and the host LBO glass matrix. The decrease in the full width at half maximum (FWHM) of the Bragg peaks suggest that there is an increase in the crystallite size. Based on this observation, it has been confirmed in these samples that the formation of samarium-doped perovskite SBN phase takes place via an intermediate fluorite-like phase. This crystallized sample has lost their transparency completely. Nanocrystallization of perovskite SBN phase via the fluorite phase has been demonstrated and studied for its electrical and optical properties which includes second harmonic generation when they are crystallized from their corresponding amorphous phase [22,23].

In order to study the influence of samarium doping on the crystal structure of SBN, we have recorded the XRD patterns for the samples heat treated at 650 °C/3 h of all the glass compositions under study, and the results are shown in Fig. 4. The substitution of Sm_2O_3 for Bi_2O_3 leads to the single phase layered SBN perovskite structure and also slightly shifts the 100% intensity peak of SBN towards higher angles which may be due to the difference in the ionic radii of Sm^{3+} (0.098 nm) and Bi^{3+} (0.103 nm) ions. Since the crystallization of the base glass matrix occurs along with the perovskite SBN phase, the Bragg peaks corresponding to the LBO phase are also seen in all these XRD patterns. The crystallite sizes (d_{sch}) estimated based on the crystalline planes (115), (200), (220), and (311) by Scherrer analysis are given

in Fig. 4. The size is in the range of 22–45 nm, confirming the nanocrystallization of un-doped and samarium-doped perovskite $SrBi_2Nb_2O_9$ phase. The crystallite size initially increases with the increase in Sm_2O_3 content (x) and reaches the value of about 45 nm at $x = 0.10$, and further substitutions result in the decrease of the crystallite size.

The incorporation of samarium in SBN lattice has a significant influence on the lattice parameters. The lattice parameters which were calculated from d-values based on the XRD data by using standard deviation method for each composition are shown in Fig. 5. The lattice constants a and b decrease with the increase in Sm_2O_3 content until $x = 0.10$ and subsequently they tend to be increasing with the increase in Sm_2O_3 content. On the other hand, the lattice parameter c shows an increasing trend when the concentration of Sm_2O_3 is lower than $x = 0.10$ and then it starts decreasing with further increase in x. It is interesting to note the variation of the lattice parameters a and b with respect to samarium concentration in the present study as generally the physical properties of layered ferroelectric compounds are significantly influenced by the polar axis (i.e., a- or b-axis) as compared to that of non polar c-axis. These lattice parameters were used to calculate the structural distortion parameters such as orthorhombicity $[2(a–b)/(a+b)]$ and tetragonal strain (c/a), and the results are shown in Fig. 6. It is noticed in Fig. 6 that the orthorhombicity increases with the substitution of Sm_2O_3 for Bi_2O_3. On the other hand the tetragonal strain increases up to 10 mol% Sm_2O_3 and thereafter it decreases as the samarium concentration is increased.

It is known that there is an extensive cation place exchange between the Bi^{3+} and Sr^{2+} ions in the crystal structure of SBN [24,25]. Some of the recent studies [18,26] on the rare-earth doped bismuth layered ferroelectric ceramics imply that rare-earth ions can substitute either in the pseudo-perovskite block or in the bismuth layer. Even though, our intention of the present study has been to substitute rare-earth ion (Sm^{3+}) in the Bi^{3+} site of $(Bi_2O_2)^{2+}$ layer, we believe that some amount of samarium ions

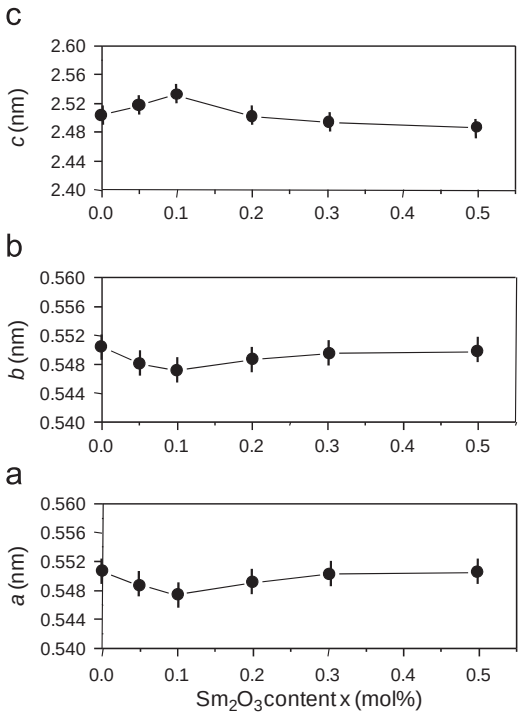

Fig. 5. Variation of lattice constants of perovskite-type SBN crystals as a function of Sm_2O_3 content in the crystallized (650 °C, 3 h) samples. (a), (b), and (c) are the lattice constants of a-, b-, and c-axes, respectively.

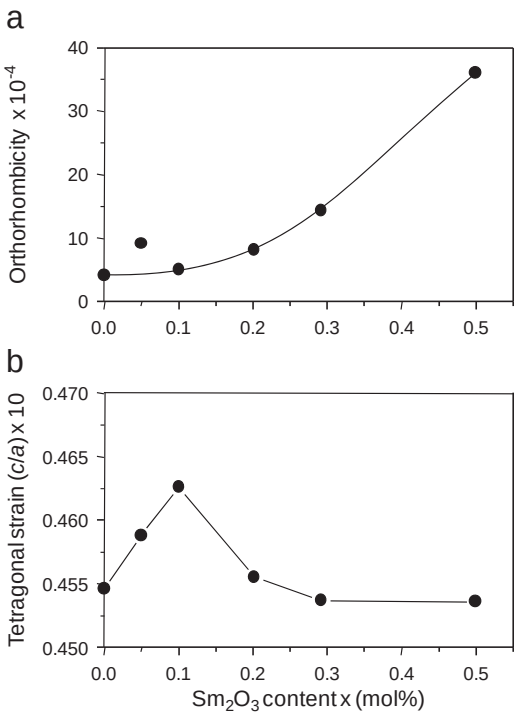

Fig. 6. Variation of (a) orthorhombicity and (b) tetragonal strain with Sm content in $SrBi_{2-x}Sm_xNb_2O_9$ perovskite phase crystallized (650 °C, 3 h) samples.

may also occupy the available Sr^{2+} sites (i.e., A-site cation) in the perovskite-like layers of SBN. This statement may be tentatively explained in the following manner. Normally, the structural stability of the bismuth layered ferroelectric compounds could be determined based on the "tolerance factor (t)" of pseudo-perovskite block. The tolerance factor is given by the following relation, $t = (r_A + r_O)/\sqrt{2}(r_B + r_O)$, where r_A, r_B and r_O are the ionic radii of A-site cation, B-site cation and an oxygen ion, respectively, and the value of "t" for the pseudo-perovskite block of $SrBi_2Nb_2O_9$ is 0.98. Since the ionic size of samarium is comparatively smaller than that of the strontium, it is highly probable that samarium ion can also enter onto the strontium sites and as a consequence the increasing concentration of samarium ion in Sr^{2+} site of perovskite-like layers will decrease the tolerance factor which makes the SBN crystal structure unstable. Hence the A-site cation can accept the samarium ion only to a certain extent in order to prevent the further decrease in the value of the tolerance factor and also to maintain the structural stability of SBN. The initial decreasing trend in the lattice parameters a and b in Fig. 5 suggest that there are some possibilities for samarium ions entering into the A-sites of pseudo-perovskite block as the samarium concentration of $x \leqslant 0.1$. We also believe that the increasing and the decreasing trend of the lattice strain in Fig. 6 could be due to the substitution of Sm^{3+} ions in the available Sr^{2+} sites of the perovskite SBN blocks when $x \leqslant 0.10$ and the Sm^{3+} substituting Bi^{3+} in Bi_2O_2 layers when $x \geqslant 0.10$. This statement is also supported by the literature report that the substitution of rare-earth ions in perovskite blocks of the similar families of layered ferroelectric compounds will cause more distortion than that of the substitution in Bi_2O_2 layer [26].

Fig. 7 shows the transmission electron micrographs and the SAED patterns obtained for the as-quenched glass and heat treated (530 °C/3 h) sample of the representative composition of $x = 0.1$. The micrograph recorded for the as-quenched glass confirms its over all amorphous nature. But the presence of nearly sharp spherical rings around the bright central region in

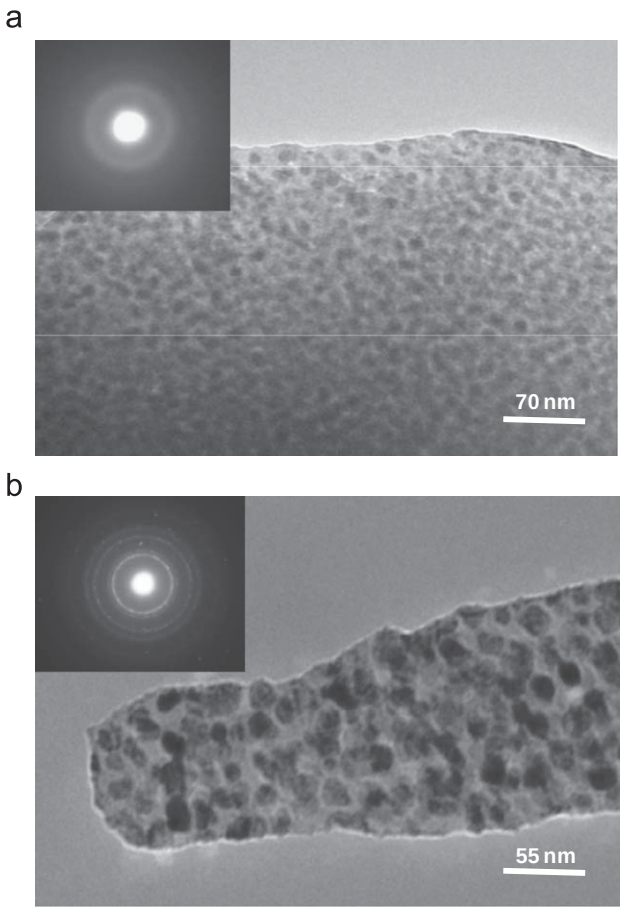

Fig. 7. Transmission electron micrographs and SAED (inset) patterns for the as-quenched (a) and (b) heat treated (530 °C, 3 h) glass samples of the composition $x = 0.1$.

the corresponding SAED pattern suggests the existence of local ordered regions (≈7 nm sized crystallites) in the LBO glass matrix. The micrograph recorded for the sample heat treated at 530 °C/3 h clearly demonstrates the distribution of fine spherical crystallites, and the average size of these crystallites is found to be around 15 nm. The SAED pattern reveals the existence of distinct diffraction rings which shows the strong crystallinity in the heat treated sample. The calculated *d*-values (0.313, 0.280, 0.198, and 0.161 nm) from the SAED pattern are in good agreement with those obtained by XRD studies confirming the formation of fluorite-like phase of $SrBi_{1.9}Sm_{0.1}Nb_2O_9$. Therefore, it is concluded that the broad peaks that were encountered in the corresponding XRD pattern (Fig. 3) are mainly due to the presence of these fine crystallites embedded in the LBO glass matrix.

3.3. Micro-Raman studies

The micro-Raman scattering spectra obtained for the as-quenched glasses in the 250–1500 cm^{-1} range are shown in Fig. 8. In the case of un-doped glass sample, the Raman peaks that are encountered at 580 and 798 cm^{-1} may be assigned to the NbO_6 octahedra. There is a noticeable upward shift of about 16 cm^{-1} in the peak position of 798 cm^{-1} with the substitution of Sm_2O_3 for Bi_2O_3 which might be due to the increase in the distortion of NbO_6 octahedra by the incorporation of smaller Sm^{3+} ions into the Bi^{3+} sites. In addition to this, the peaks observed at 434 and 501 cm^{-1} are close to those reported for SBN sample [27,28]. The peaks at 657 and 1060 cm^{-1} would be attributed to the base LBO glass matrix [27]. The micro-Raman scattering

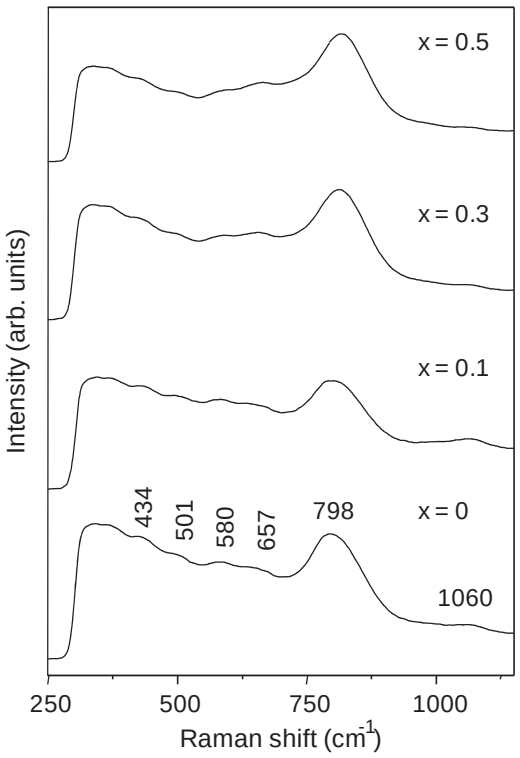

Fig. 8. Raman scattering spectra at room temperature for the as-quenched glass samples of various compositions of *x*.

spectra are also measured for the samples heat treated at 530 °C for 3 h of all the compositions. Several broad peaks are observed, and those peaks are assigned to fluorite-like SBN nanocrystals [27]. The details pertaining to the Raman studies of fluorite-like phase un-doped and samarium-doped strontium bismuth niobate have been reported elsewhere [29].

Fig. 9 shows the Raman scattering spectra recorded for the crystallized (650 °C) samples of various compositions of *x*. The broad Raman peaks at 441, 577, and 837 cm^{-1} indicate the formation of perovskite type SBN nanocrystals [27]. The characteristic Raman features of SBN nanocrystals are at 577 and 837 cm^{-1}, which corresponds to the E_g (involving opposing excursions of the epical oxygen atoms of the octahedral) and A_{1g} modes (symmetric stretching of the NbO_6 octahedra). Apart from this, there are also less intense peaks seen in the Raman spectra, which are assigned to the base LBO glass matrix. These observations suggest that, as the heat treatment temperature is increased to 650 °C, the fluorite-like SBN phase is completely transformed to the perovskite phase.

The substitution of Sm_2O_3 for Bi_2O_3 has shown some strong influence on the Raman peak positions in the crystallized (650 °C) samples, and the peak positions of the A_{1g} mode is shown in Fig. 10 as an example. It is seen that the A_{1g} mode tends to shift towards higher Raman frequencies as $x \leqslant 0.1$ and thereafter it starts decreasing with further increase in *x*. This behavior is consistent with that of the variation in the tetragonal strain in the present study as shown in Fig. 6. The above observation suggests that the vibrational frequency of the NbO_6 octahedra is greatly influenced by the lattice strain. The observed shift of the Raman frequencies could also be due to the difference in the atomic mass of samarium and bismuth atoms.

The variation of the full width at half maximum of the peak of the A_{1g} mode is shown in Fig. 10, indicating that the FWHM values are also influenced by the Sm_2O_3 content. It is known in the literature that the FWHM of the Raman bands could be related to

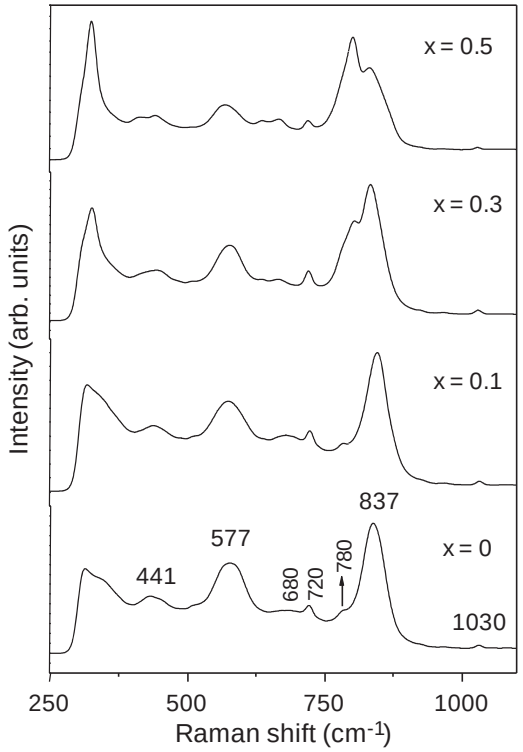

Fig. 9. Raman scattering spectra at room temperature for the crystallized (650 °C, 3 h) samples of various compositions of *x*.

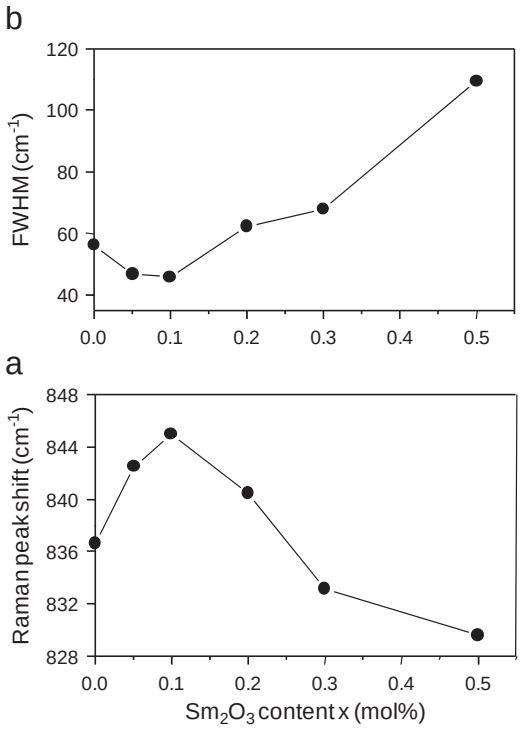

Fig. 10. Raman shift (a) and FWHM (b) of the A_{1g} mode observed in perovskite-type SBN nanocrystals formed in the crystallized (650 °C, 3 h) samples as functions of Sm_2O_3 content.

the degree of order of the cations in the lattice [30] (i.e narrower the band, the higher will be the ordering in the lattice and vice versa). The observed line broadening of the Raman band of the A_{1g} mode from $x = 0.10$ in the present study may be attributed to the random distribution of Bi^{3+} and Sm^{3+} cations in the Bi_2O_2 layer of SBN structure. Apart from this, the decreasing trend in the crystallite size of the embedded perovskite SBN like phase as the samarium concentration increases from $x = 0.10$ would have also influenced the broadening of the corresponding Raman band. On the other hand, the peak position of the E_g mode was found to be almost constant irrespective of the Sm_2O_3 content. Furthermore, It is noted that the intensity of the Raman peak corresponding to the LBO phase (i.e. 780 cm^{-1}) increases with the increase in samarium content and also the peak position shifts towards higher frequency side with the substitution of Sm_2O_3 for Bi_2O_3.

Table 1
Values of the dielectric constant at 100 kHz for the heat treated samples of the compositions $x = 0$ and 0.1.

Heat treatment temperature (°C)	Dielectric constant at 100 kHz	
	$x = 0$	$x = 0.1$
460	23	26
500	29	31
530	34	35
550	42	46
650	47	58

3.4. Dielectric studies of glasses and glass nanocrystal composites

The dielectric constant (ε_r) measurements have been carried out at the frequency of 100 kHz at room temperature on the heat treated samples for the representative composition $x = 0.1$ and the corresponding values are listed in Table. 1. It is seen that the dielectric constant increases gradually with the increase in heat treatment temperature and attains the value of $\varepsilon_r \approx 58$ for the crystallized (650 °C) sample and this observation is akin to those reported in the literature for similar families of layered ferroelectric oxides dispersed in lithium borate glasses [31]. This clearly reveals that the dielectric constant of perovskite type SBSmN nanocrystals is relatively larger than that of the corresponding fluorite-like nanocrystals and the precursor glass. For the sake of comparison, the values of the dielectric constant with the heat treatment temperature for the un-doped samples (i.e. $x = 0$) are also given in Table. 1. Even in the case of un-doped samples, a gradual increase in ε_r is observed similar to the case of samarium-doped samples. However, it should be pointed out that the values of ε_r in all the range of heat treatment temperatures are slightly lower than those of the samarium-doped ($x = 0.1$) samples, indicating that the incorporation of samarium into the SBN lattice increases the dielectric polarization. The dielectric loss (D) is also one of the key parameters for practical applications. For instance, the samples heat treated at 530 °C for 3 h give the values of $D \sim 0.06$ in $x = 0$ and $D \sim 0.05$ for $x = 0.1$ at 100 kHz [29]. More detailed studies on the dielectric loss and relaxation mechanism for the samples prepared in this study are now under consideration.

4. Conclusions

The nanocrystallization of the perovskite phase of un-doped and samarium-doped strontium bismuth niobates was confirmed via the fluorite phase formation in $16.66SrO–16.66[(1-x)Bi_2O_3–xSm_2O_3]–16.66\ Nb_2O_5–50\ Li_2B_4O_7$ ($0 \leqslant x \leqslant 0.5$) glasses. It was found that the substitution of Sm_2O_3 for Bi_2O_3 has a significant influence on the lattice parameters of orthorhombic SBN crystal structure. The dielectric constant, which is an

important property to be considered in the design and fabrication of polar devices, could be tailored by controlling the microstructure (crystallite size). Interestingly, the dielectric constants of the glass composites comprising of perovskite-type un-doped and samarium-doped SBN nanocrystals were higher than those of fluorite-like crystals.

Acknowledgments

This work was supported by a Grant-in-Aid for Scientific Research from the Ministry of Education, Science, Sports, Culture and Technology, Japan. The authors also thank Prof. H. Suematsu and Mr. T. Suzuki for TEM observation experiments.

References

[1] H. Gleiter, J. Appl. Crystallogr. 24 (1991) 79.
[2] F. Cardellini, V. Contini, G. Mazzone, A. Montone, Philos. Mag. B 76 (4) (1997) 629.
[3] R.W. Seigel, Sci. Am. 275 (1996) 42.
[4] N.F. Borelli, J. Appl. Phys. 38 (1967) 4243.
[5] K. Tanaka, K. Kahima, N. Soga, A. Mito, H. Nasu, J. Non-Cryst. Solids 185 (1995) 123.
[6] T. Komatsu, H. Tawarayama, H. Mohri, K. Matusita, J. Non-Cryst. Solids 135 (1991) 105.
[7] N. Toyohara, Y. Benino, T. Fujiwara, T. Komatsu, Solid State Commun. 140 (2006) 299.
[8] Y. Takahashi, Y. Benino, T. Fujiwara, T. Komatsu, Appl. Phys. Lett. 81 (2002) 223.
[9] M.V. Shanker, K.B.R. Varma, J. Non-Cryst. Solids 226 (1998) 145.
[10] G. Senthil Murugan, G.N. Subbanna, K.B.R. Varma, J. Mater. Sci. Lett. 18 (1999) 1687.
[11] B. Aurivillius, Ark. Kemi 1 (1951) 449.
[12] J.F. Scott, C.A.P. De Araujo, Science 246 (1989) 1400.
[13] S.B. Desu, D.P. Vijay, Mater. Sci. Eng. B 32 (1995) 75.
[14] C.A.P. De Araujo, J.D. Cuchlaro, L.D. Mc Millan, M.C. Scott, J.F. Scott, Nature 374 (1995) 627.
[15] T. Mihira, H. Yoshimori, H. Watanabe, C.A.P. De Araujo, Jpn. J. Appl. Phys. 34 (1995) 5233.
[16] P. Millan, A. Ramirez, A. Castro, J. Mater. Sci. Lett. 14 (1995) 1657.
[17] P. Millan, A. Castro, J.B. Torrance, Mater. Res. Bull. 28 (1993) 117.
[18] A. Srinivas, T. Sritharan, F.Y.C. Boey, J. Appl. Phys. 98 (2005) 036104.
[19] S. Sakka, J.D. Mackenzie, J. Non-Cryst. Solids 6 (1971) 145.
[20] T. Asai, E.R. Camargo, M. Kakihana, M. Osada, J. Alloys Compd. 309 (2000) 113.
[21] Ismunandar, B.J. Kennedy, Gunawa, Marsongkohadi, J. Solid State Chem. 126 (1996) 135.
[22] N. Syam Prasad, K.B.R. Varma, J. Nanosci. Nanotech. 1 (2001) 425.
[23] N. Syam Prasad, K.B.R. Varma, Y. Takahashi, Y. Benino, T. Fujiwara, T. Komatsu, J. Solid State Chem. 173 (2003) 209.
[24] A.D. Rae, J.G. Thompson, R.I. Withers, Acta Crystallogr. Sect. B Struct. Sci. 48 (1992) 418.
[25] S.M. Blake, M.J. Falconer, M.C. Creedy, P. Lightfoot, J. Mater. Chem. 7 (1997) 1609.
[26] J. Zeng, Y. Li, D. Wang, Q. Yin, Solid State Commun. 133 (2005) 553.
[27] N. Syam Prasad, K.B.R. Varma, Mater. Sci. Eng. B 90 (2002) 246.
[28] P.R. Graves, G. Hua, S. Myhra, J.G. Thompson, J. Solid State Chem. 114 (1995) 112.
[29] B. Harihara Venkataraman, T. Fujiwara, K.B.R. Varma, T. Komatsu, Mater. Chem. Phys, under review.
[30] D. Rout, V. Subramanian, K. Hariharan, V. Sivasubramanian, Solid State Commun. 141 (2007) 192.
[31] C. Karthik, K.B.R. Varma, J. Non-Cryst. Solids 353 (2007) 1307.